Materials Science & Engineering A 911 (2024) 146907

Contents lists available at ScienceDirect

Materials Science & Engineering A

journal homepage: www.elsevier.com/locate/msea

# Synchrotron X-ray diffraction studies of the internal load transfer in Ni–CrC metal matrix composites

Jianxiong Li [a], Katherine S. Shanks [b], Amlan Das [b], Isaac M. Nault [c], Mostafa Hassani [a,d,*]

[a] Sibley School of Mechanical and Aerospace Engineering, Cornell University, Ithaca, NY, 14850, USA
[b] Cornell High Energy Synchrotron Source, Cornell University, Ithaca, NY, 14850, USA
[c] U.S. Army Research Laboratory, Weapons and Materials Research Directorate, Aberdeen Proving Ground, MD, USA
[d] Department of Materials Science and Engineering, Cornell University, Ithaca, NY, 14850, USA

ARTICLE INFO

*Keywords:*
Metal matrix composites
Ni–CrC
Synchrotron X-ray diffraction
Internal load transfer
Cold spray

ABSTRACT

Strengthening in metal matrix composites (MMCs) is primarily due to the load transfer from the compliant matrix to the stiff reinforcement. While internal load transfer has been studied for conventionally manufactured MMCs, the extent to which it may be affected by the preexisting defects in additively manufactured MMCs remain elusive. In this study, we performed uniaxial compression loading on cold sprayed Ni–CrC particulate-reinforced MMC. We observe significantly enhanced strength and ductility compared to the brittle behavior previously reported in tension for the same MMC. In contrast to the absence of load transfer in tension, the presence of initial defects did not preclude the internal load transfer in the composites under compressive loading. In-situ high-energy X-ray diffraction analysis revealed a relatively constant load partitioning in the elastic regime, which aligned well with predictions by the Eshelby's inclusion model. Furthermore, an internal load transfer was observed from the Ni matrix to the CrC reinforcement upon plastic deformation of the Ni matrix. Finite element modeling further confirmed this and demonstrated that localized tensile stress at the interface in the transverse direction resulted in the interfacial debonding and partial relaxation of the matrix. We also report reinforcing particle fracture upon further compression which in turn triggered the eventual failure of the MMC.

## 1Introduction

Metal matrix composites (MMCs), usually composed of a ductile base metal reinforced with a stiff ceramic phase, offer enhanced strength and stiffness compared to pure metals and higher ductility compared to pure ceramics [1]. Such a favorable combination of properties has inspired interest in using MMCs for various applications, such as biomedical, automotive and aerospace structures [1–5]. However, MMCs entail more complicated strengthening and failure mechanisms compared to monolithic materials, primarily due to the significant physical and mechanical property disparities between the metal matrix and the ceramic reinforcements [1]. What is more, internal load transfer from the matrix to the reinforcement is a critical phenomenon affecting both strengthening and failure of MMCs. The dominant MMC failure mechanisms include matrix ductile failure, interfacial debonding, and reinforcement fracture [6–10].

Particulate-reinforced MMCs with different matrices and reinforcement contents exhibit different threshold stresses for internal load transfer. Generally, MMCs with Body Centered Cubic (BCC) and Hexagonal Close Packed (HCP) metal matrices such as steel-based and Ti-based MMCs display higher load transfer initiation stress and failure stresses when compared to MMCs with Face Centered Cubic (FCC) counterparts such as Al-based MMCs [11–20]. This distinction arises from the superior yield strength and stiffness of BCC and HCP metal matrices in comparison to the FCC counterparts. Consequently, the internal load transfer, potential debonding of matrix/ceramic particles, and cracking of ceramic particles are delayed until higher stress levels.

Beyond the influences stemming from the mechanical properties of the matrix and reinforcements, the impact of incipient defects in composites and defects generated during loading on internal load transfer and failure mechanisms remains uncertain. Some studies found that the incipient damage in the particles would cause early termination of the internal load transfer [21,22]. However, slight load transfer from the metallic matrix to ceramic reinforcements was also reported even after early relaxation of ceramic reinforcements [23]. When the ceramic damage evolves at higher stresses, load fraction borne by the ceramic

* Corresponding author. Sibley School of Mechanical and Aerospace Engineering, Cornell University, Ithaca, NY, 14850, USA.
*E-mail address:* hassani@cornell.edu (M. Hassani).

https://doi.org/10.1016/j.msea.2024.146907
Received 19 October 2023; Received in revised form 21 March 2024; Accepted 30 June 2024
Available online 1 July 2024
0921-5093/© 2024 Elsevier B.V. All rights are reserved, including those for text and data mining, AI training, and similar technologies.

phases was reported to continuously decrease whereas the load fraction borne by the metal matrix increased. On the other hand, Roy et al. [24] reported saturation of the load fraction borne by ceramic reinforcements together with continuous decrease in the load fraction borne by the metal matrix at high stresses. These seemingly disparate findings call for a thorough understanding of how defects influence the internal load transfer and failure mechanisms of MMCs. This understanding is essential not just for the extensively studied Al-based, Ti-based, and steel-based metal matrix composites [18,25–31] but also for more recently developed nickel-based composites offering strengths comparable with steel-based metal matrix composites and pushing the property envelope for MMCs with pure FCC metallic matrices (See Supplementary Fig. S3). Ni-based MMCs also offer potential applications for cutting tools, wearing plates, pistons, and turbine blades [32–37].

In our previous work on cold-sprayed Ni–CrC MMCs [21], we used high energy synchrotron X-ray diffraction to study the load transfer and damage mechanisms under uniaxial tension. Our results showed linear elastic responses for both phases all the way to the final fracture. Neither plasticity within the Ni matrix nor load transfer between the two phases occurred during tensile loading. We concluded that the lack of plasticity and load transfer in our composites leading to a premature brittle fracture is the result of the preexisting defects in the material produced during the spraying process.

In this paper we turn to the behavior of the cold sprayed Ni–CrC MMCs under compression. The study was motivated by the fact that the metal matrix composite is less sensitive to the presence of the preexisting defects during compression. More extensive deformation together with micro- and macro-plasticity are achievable under compression enabling studies of the damage processes. From an applied point of view, understanding the compressive behavior of Ni–CrC is critical, particularly for the conditions under which these composites are used in the form of protective structural coatings [33,34,36]. Here we conducted in-situ uniaxial compression tests on Ni–CrC composite with synchrotron X-ray diffraction to study the internal load transfer and failure mechanisms in an extended range of plastic deformation. We also used the Eshelby's equivalent inclusion model to predict the stress partitioning between the matrix and reinforcements in the composite. What is more, we have developed a finite element model to justify and support our experimental observations.

## 2. Materials and experiments

### 2.1. Cold spray

Feedstock containing a blend of gas atomized pure Ni and agglomerated CrC–NiCr composite powder particles was purchased from Solvus Global (Worcester, MA, USA). The blend ratio was 25 % Ni and 75 % CrC–NiCr by mass. Since the CrC–NiCr particles are rich in CrC (~90 % volume fraction), we refer to them as 'CrC' particles in the reminder of the text. The morphology of the powder particles used in this study is shown in Fig. 1a (Ni powder) and Fig. 1b (CrC powder). The Ni and CrC powder particles have mean sizes of 34 μm and 37 μm, respectively. The composite was deposited onto a steel substrate using a VRC Gen III Max cold spray system. Helium carrier gas was used with a VRC powder feeder and a VRC NZZL0058 nozzle. The cold spray parameters are reported in Table 1. The process produced composites with uniform distribution of reinforcing particles, shown in Fig. 1c. The volume fractions of the reinforcement in the deposit were measured to be 35 %. However, it is also evident from Fig. 1c that defects are present, highlighted with the red arrows. The defects are mainly in the form of imperfectly bonded areas and cracks withing the reinforcement. More details on the microstructure, phase, chemical composition, and defect distribution are available in our previous publication [21].

### 2.2. Microstructural characterizations

We used a wire electric discharge machine (EDM) to extract samples from the cold spray deposits for microstructural characterizations. Following standard metallographic sample preparation steps, the deposit's surfaces and cross-sections were ground and polished to a nominally 0.04 μm mirror finish. We conducted microstructural characterizations using a Tescan Mira3 Field Emission Scanning Electron Microscope (SEM) (Brno, Czech Republic). After the uniaxial compression experiments described below were completed, the failed specimens were also cross sectioned in the longitudinal (loading) direction, ground, and polished to mirror finish for further failure characterizations with SEM.

### 2.3. In-situ high energy X-ray diffraction (HEXRD)

We conducted *in-situ* High Energy X-Ray Diffraction (HEXRD) measurements during uniaxial compression at beamline ID3A of the Cornell High Energy Synchrotron Source (CHESS). Fig. 2 shows the experimental setup for the HEXRD measurements and the dimensions of the specimens. Two uniaxial loading specimens were prepared with a

**Table 1**
Spraying conditions of the cold spray process.

| Spray Gas | Pressure (bar) | Temperature (°C) | Main Gas Flow Rate (L/min) | Carrier Gas Flow Rate (L/min) |
|---|---|---|---|---|
| Helium | 29–31 | 620–630 | 1100–1300 | 140–160 |

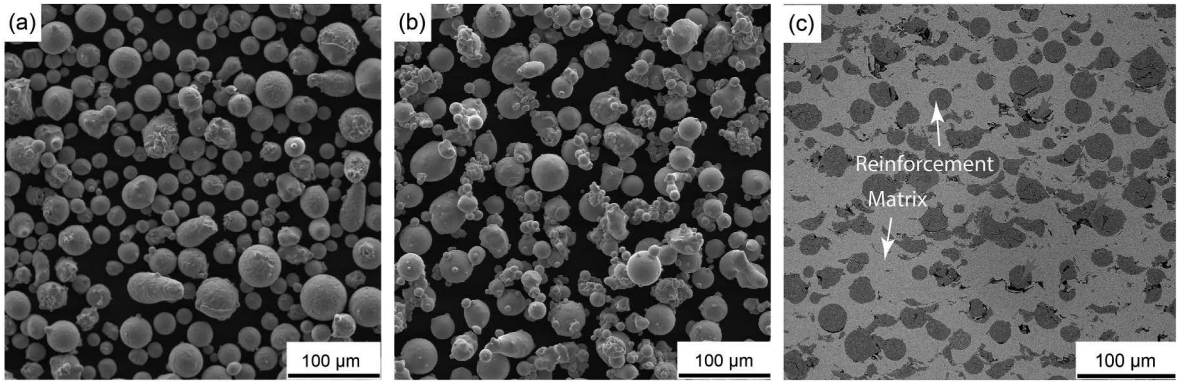


**Fig. 1.** Ni (a) and CrC (b) powder feedstock used in the cold spray process. Both powders show a generally spherical morphology. In (c), where the cross-sectional microstructure of the deposit is shown, a uniform distribution of CrC reinforcement (dark-colored particles) is achieved during the spraying process. Defects including pores and cracked particles are shown with red arrows in (c). (For interpretation of the references to color in this figure legend, the reader is referred to the Web version of this article.)

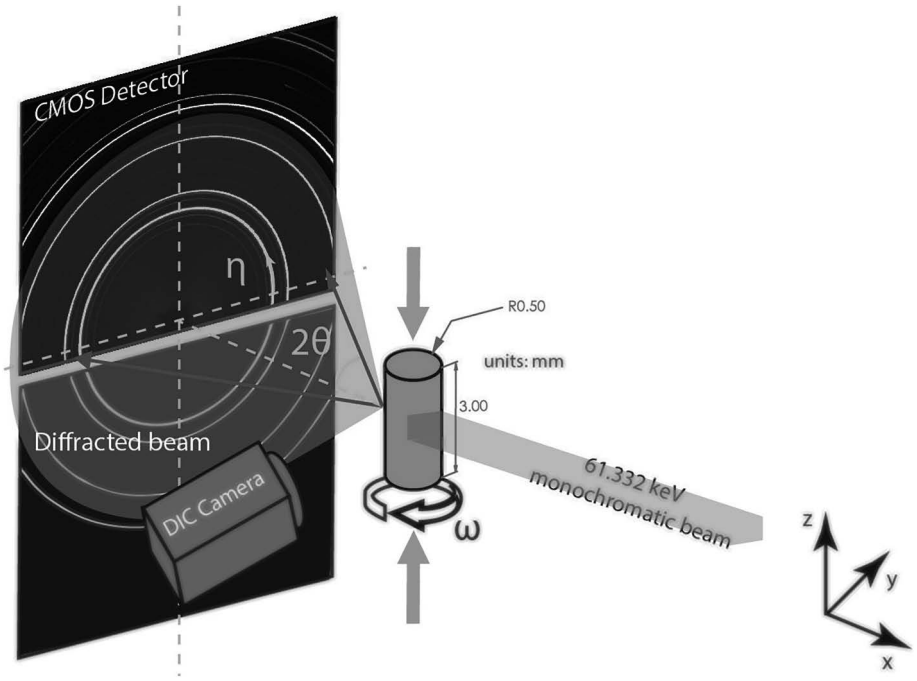


**Fig. 2.** A schematic of the in-situ synchrotron X-ray diffraction experiments as well as the geometry of the specimens used in this work.

diameter of 1 mm and a length of 3 mm. The samples were extracted so that the loading direction ($z$) was along the cold spray build direction. The uniaxial loading was conducted on the Cornell Compact Load Frame (CCLF) in a displacement-controlled fashion, with a quasistatic deformation rate and a 1 μm displacement (0.033 % engineering strain) increment of the platens. Macroscopic strains were measured after each displacement increment using digital image correlation (DIC). The loading was interrupted at stress increments of 100 MPa for HEXRD measurements with a monochromatic X-ray beam with an energy of 61.332 keV, a height of 1 mm, and a width of 2.2 mm, covering the entire width of the specimens. Two Dexela 2923 detectors with 3888 × 3072 pixels each and 74.8 μm pixel sizes were used for the data acquisition. The sample-to-detector distance was calibrated to 880 mm using $CeO_2$ standard reference powder. The top detector is placed to cover azimuthal angles, $\eta$, from 0 to 180°, while the bottom detector is placed lower to cover $\eta$ values from 181 to 360°. Arrangement of the detectors allows the collection of diffraction angles ($2\theta$) of up to 12 degre(es in the z-direction and 9.5° in the y-direction. For each load increment, diffraction data were acquired at 0.25-degree intervals with an exposure time of 0.35 s when the sample covered a rotation angle, $\omega$, of 360° about the z-axis.

Details of diffraction data analysis are reported in our earlier work [21]. Diffracted peak positions ($2\theta$), widths, and intensities were determined for each peak. Average elastic lattice strain corresponding to a particular peak ($hkl$), at a given load step was then calculated using Eq. (1):

$$\varepsilon = \frac{d}{d_0} - 1 = \frac{\sin\theta_0}{\sin\theta} - 1 \tag{1}$$

where $d$ and $d_0$ are the lattice spacing of a given crystallographic plane in the unstrained and strained state, and $\theta_0$ and $\theta$ are the Bragg angles of an individual peak in the unloaded and loaded states, respectively. This process was repeated for all peaks of interest at all angles of rotation and load steps. Since the results for the two specimens were similar within the experimental error (~10 %), only one set of HEXRD results is presented.

### 2.4. Theory

The phase specific stresses in metal matrix composites under an applied stress can be calculated by the Eshelby's equivalent inclusion model [16,38–42]. In this model, the total MMC stress, $\overline{\sigma}$, determined from a measured strain, $\varepsilon$, for each phase in the composite is composed of three components. The first component, $\sigma^A$, represents the applied stress and remains the same for both the metal and ceramic phases. The second component is the elastic stiffness misfit stress, $\overline{\sigma}_{misfit}$, which quantifies the extent of load transfer from the metal matrix to the reinforcement due to the applied stress. The third component is the shape misfit stress, $\sigma^{sh}_{misfit}$, which accounts for the thermal and plastic misfits. When calculating the stress partitioning during the elastic deformation stage under external loading, this last component can often be neglected [42].

At equilibrium, the sum of the volume averaged total stresses for each phase should be equal to the applied stress:

$$(1-f)\overline{\sigma}_M + f\overline{\sigma}_R = \sigma^A \tag{2}$$

Where $f$ is the volume fraction of reinforcements, and $\overline{\sigma}_M$ and $\overline{\sigma}_R$ are the volume averaged stresses for the metal matrix and the reinforcement, respectively. $\overline{\sigma}_M$ and $\overline{\sigma}_R$ can be expressed by a superposition of the applied stress, $\sigma^A$, and the elastic stiffness misfit stress, $\overline{\sigma}_{misfit}$, as follows:

$$\overline{\sigma}_M = \sigma^A + \overline{\sigma}_{M,misfit} \tag{3}$$

$$\overline{\sigma}_R = \sigma^A + \overline{\sigma}_{R,misfit} \tag{4}$$

Where $\overline{\sigma}_{M,misfit}$ and $\overline{\sigma}_{R,misfit}$ are the elastic stiffness mismatch stresses for the metal matrix and reinforcement, respectively.

The elastic misfit stresses for the matrix and reinforcement are proportional to the applied stress [18,20]:

$$\overline{\sigma}_{M,misfit} = \boldsymbol{B_M}\sigma^A \tag{5}$$

$$\overline{\sigma}_{R,misfit} = \boldsymbol{B_R}\sigma^A \tag{6}$$

Where $\boldsymbol{B_M}$ and $\boldsymbol{B_R}$ depend on the elastic constants of both phases as well

as aspect ratio and volume fraction of the reinforcements [18,42]:

$$\boldsymbol{B_M} = f\boldsymbol{C_M}(\boldsymbol{S}-\boldsymbol{I})\{(\boldsymbol{C_M}-\boldsymbol{C_R})[\boldsymbol{S}-f(\boldsymbol{S}-\boldsymbol{I})]-\boldsymbol{C_M}\}^{-1}(\boldsymbol{C_M}-\boldsymbol{C_R})\boldsymbol{C_M}^{-1} \quad (7)$$

$$\boldsymbol{B_R} = -(1-f)\boldsymbol{C_M}(\boldsymbol{S}-\boldsymbol{I})\{(\boldsymbol{C_M}-\boldsymbol{C_R})[\boldsymbol{S}-f(\boldsymbol{S}-\boldsymbol{I})]-\boldsymbol{C_M}\}^{-1}(\boldsymbol{C_M}-\boldsymbol{C_R})\boldsymbol{C_M}^{-1} \quad (8)$$

Where $\boldsymbol{C_M}$ and $\boldsymbol{C_R}$ are the matrix and the reinforcement stiffness tensors, respectively; $\boldsymbol{I}$ is the identity matrix, and $\boldsymbol{S}$ is the Eshelby's tensor which is related to the Poisson's ratio of the matrix, and the shape and aspect ratio of the reinforcement [18,43,44]. We used an aspect ratio of unity for the spherical reinforcement in this work [18,42].

Finally, the load fraction borne by the metal matrix, $l_M$, and the reinforcement, $l_R$, can be calculated with Eqs. (9) and (10) respectively:

$$l_M = \frac{(1-f)\overline{\sigma}_M}{\sigma^A} \quad (9)$$

$$l_R = \frac{f\overline{\sigma}_R}{\sigma^A} \quad (10)$$

### 2.5. Finite element simulation

To further understand internal load transfer behavior and driving force for matrix/reinforcement interfacial debonding, we developed a 2D finite element model of uniaxial compression of a particulate reinforced metal matrix composite. A representative volume element (RVE), shown in Fig. 3, was created with the finite element package in ABAQUS [45] to simulate the uniaxial loading response of the composite deposit. The diameter of the embedded particle was set to 37 μm to represent the average particle size used in cold spray deposition. The dimensions of the RVE were accordingly set to 57.25 × 57.25 $\mu m^2$ square to represent the experimentally measured volume fraction of the reinforcing particles. Perfect bonding between the reinforcement and the matrix was assumed ensuring a continuous deformation at the interface.

A 12 % compressive strain was applied quasi-statically on the top boundary (see Fig. 3) and the displacement was constrained in the y direction for the bottom boundary. Periodic boundary conditions were applied to the elements on all edges of matrix by linking the deformation of respective nodes. The Ni matrix was modeled as an elastoplastic material with a linear strain hardening. The elastic modulus and the Poisson's ratio were set to 200 GPa and 0.31, respectively. Informed by the diffraction data (see next section), we applied a yield strength of 600 MPa for the Ni matrix. To reproduce the macroscopic stress-strain curve of the composites a hardening rate of 25.4 GPa and a saturation flow stress of 1082 MPa were used for the behavior of the matrix after yielding. The CrC reinforcing particle was modeled as a linear elastic material with an elastic modulus of 357.5 GPa and a Poisson's ratio of 0.3.

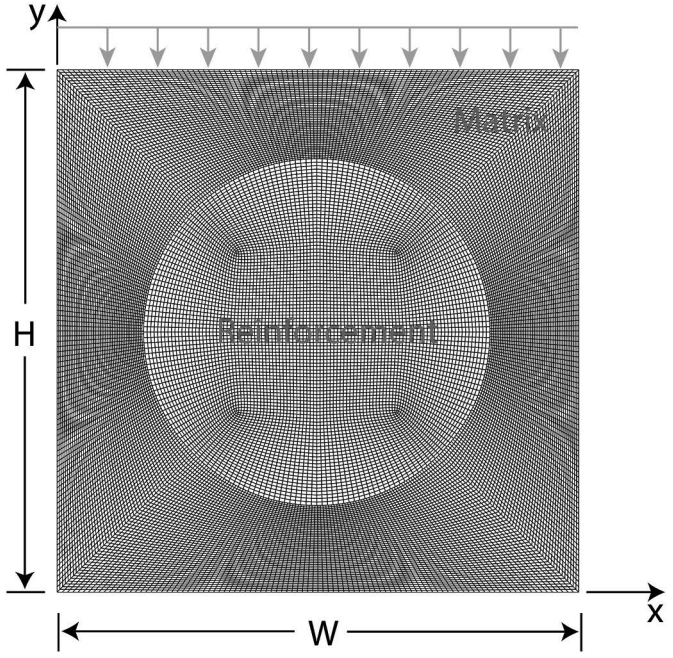


**Fig. 3.** Finite element model and discretization used in this study. H and W signify the height and width of the representative volume element which are both equal to 57.25 μm.

## 3. Results

### 3.1. Macroscopic behavior

Fig. 4 shows the MMC's macroscopic compressive true stress-strain curves. The tensile behavior from our previous study is also superimposed on the plot [21]. We measured the ultimate compressive strength of the MMC to be 1163 ± 7 MPa, almost two times higher than that under tension. Using a 0.2 % strain offset, we determined the yield strength of the composites under compression to be 809 ± 11 MPa. The composite failed at 12.1 ± 0.5 % strain, which is significantly higher than ~0.5 % failure strain reported for tension. The composite has also shown a significant level of strain hardening after yielding.

### 3.2. Microstructural observations

Fig. 5 shows the overall cross-sectional microstructures of the failed composites together with exemplar defects close to and far away from the fracture plane. It can be observed that eventual failure is shear driven at 45° relative to the loading direction. Relatively large interfacial gaps between the matrix and the reinforcing particles in the transverse direction can be observed for the particles located close to the fracture plane (Fig. 5a and c). Some particles in that region experience cracking parallel to the loading direction (Fig. 5b). Similar defects have been also reported for cold sprayed Al–$Al_2O_3$ particulate MMCs [46]. Smaller interfacial gaps or cracks can be observed in the areas far away from the fracture plane. However, no preferred orientation for the defects can be identified in regions far from the fracture plane (See Supplementary Fig. S1 for additional micrographs). This contrast in defect

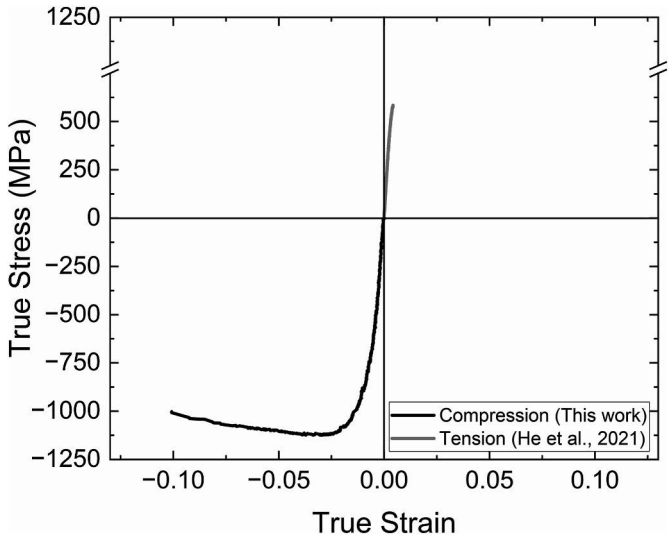


**Fig. 4.** *CS Ni–CrC MMC's Macroscopic stress-strain curve in compression and tension. The data for tension was reproduced from Ref.* [21]. *Significantly higher strength and ductility is obtained in compression.*

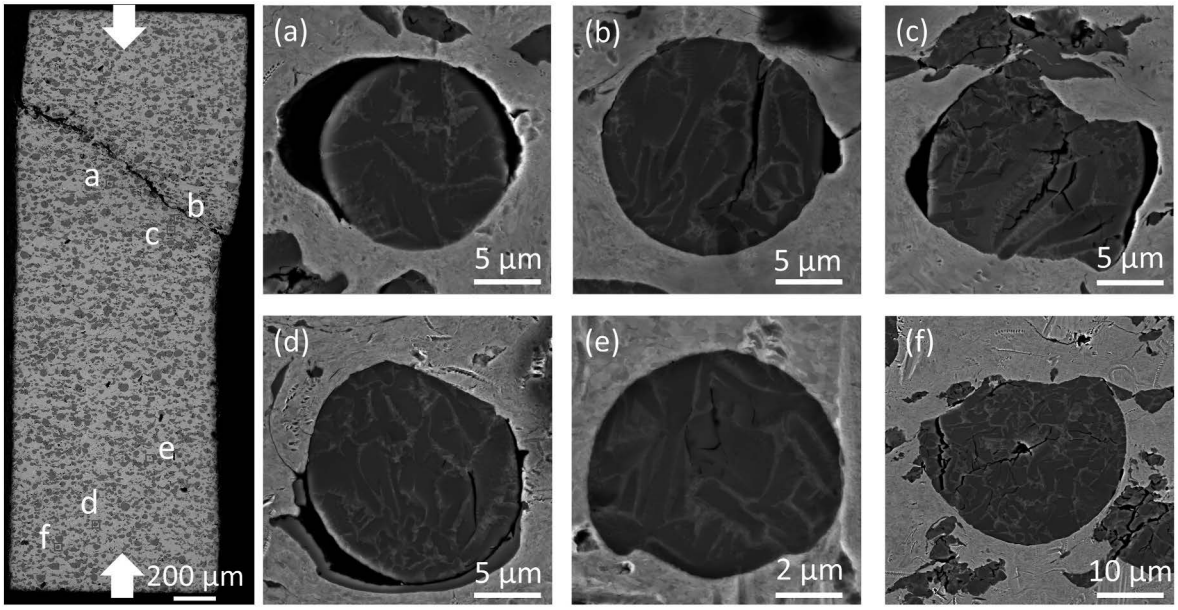


**Fig. 5.** Particles (a), (b), and (c), close to the failure surface, show detachment around and cracks inside particles parallel to the loading direction. Particles (d), (e), and (f) show more random defects mainly generated during the cold spray process. White arrows indicate the direction of loading.

orientations suggests that the defects close to the fracture plane are not pre-existing in the sprayed composite but rather produced during the loading. However, there is a possibility that the larger cracks after compression were sourced from the small preexisting cracks in the reinforcing particles which further propagated during compression.

### 3.3. In-situ X-ray diffraction

In our previous study, HEXRD results showed linear elastic behavior up to the final fracture for both Ni and CrC phases under uniaxial tension [21]. Here we observed significantly different behavior at the phase level when the composite is compressed. Fig. 6 shows the longitudinal and transverse lattice strains for Ni and CrC phases as a function of the applied stress. We choose to show only one representative plane from each phase, namely Ni (200) for nickel and CrC (420) for the carbide, as we observe similar trends for different crystallographic directions in the same phase (see Fig. S2 in Supplementary Information for an additional CrC orientation).

The evolution of the longitudinal lattice strain in Ni (200) and CrC (420) reveals distinct behavioral regimes. Initially a linear elastic response is observed from 0 to ~600 MPa in both phases (stage I). Beyond 600 MPa, the rate of longitudinal lattice strain increment for Ni

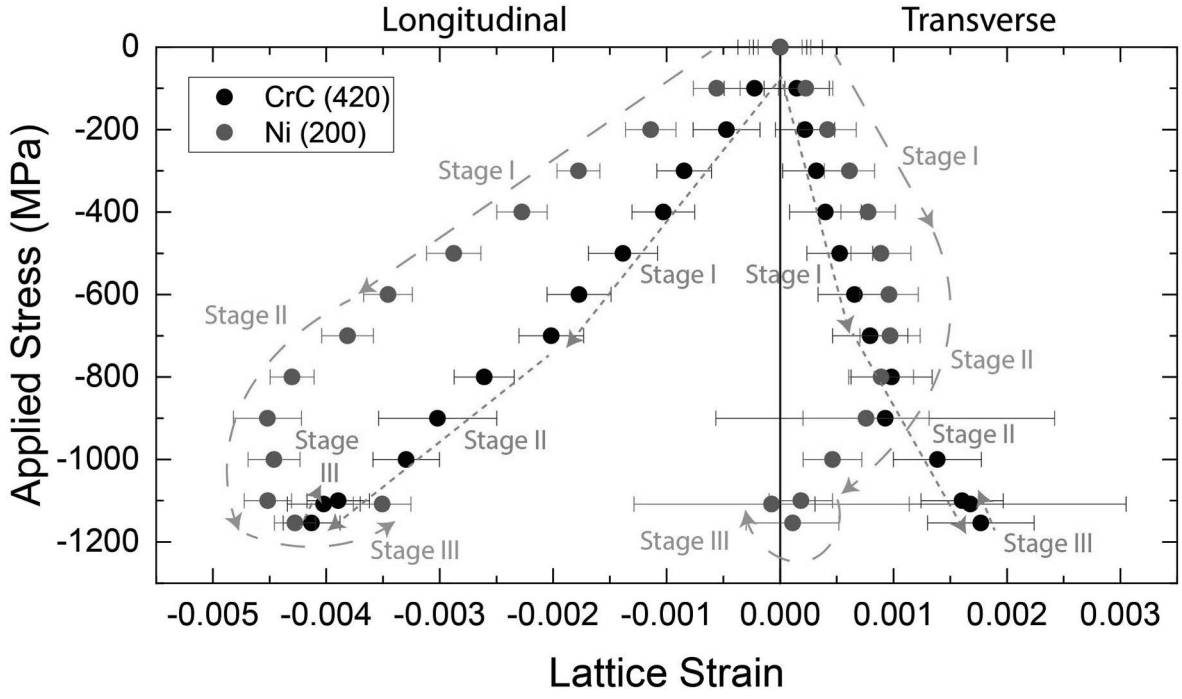


**Fig. 6.** Longitudinal and transverse lattice strains for nickel and chromium carbide phases vs. applied stress. Only one representative plane from each phase is shown due to similar behaviors observed in different planes of the same phase.

starts decreasing. This results in a plateau as the applied stress further increases (stage II). This suggests that yielding occurs in the Ni matrix at approximately 600 MPa. At the same time, we observe a change in the slope for CrC lattice strains indicating an internal load transfer from the metallic matrix to the ceramic reinforcement. The reinforcement remains elastic in stage II. As the applied stress exceeds 1150 MPa, the lattice strain in both phases begins to slightly decrease (stage III) close to the final fracture.

The longitudinal contraction is accompanied by a transverse expansion as expected; we measure positive lattice strains in both Ni and CrC phases. We observe the same three stages in the transverse lattice strain evolution in Fig. 6. What is, however, different is that after yielding there is no plateau in the Ni lattice strain. The matrix fully relaxes in the transverse direction after yielding. We attribute this transverse full relaxation to the matrix/reinforcement debonding and the creation of free surfaces as a result. This is also supported by the SEM micrographs (see Fig. 4), where we observe matrix/reinforcement interfacial debonding and free surface creation in the transverse direction. The matrix to reinforcement load transfer also occurs in the transverse direction as evident by the change in slope for the CrC transverse lattice strains.

Fig. 7 shows the full width at half maximum (FWHM) of the Ni peaks, normalized with the FWHM in the unloaded condition as a function of the applied macroscopic stress. We observe a significant increase in the FWHM at stress levels exceeding 600 MPa. This increase is in contrast to our previous work where the MMC showed no significant change in the FWHM before failure in tension [21]. The observed significant increase in FWHM beyond the applied stress of 600 MPa under compression confirms that plastic deformation occurred in the Ni matrix [47,48]. The coincidence of the increase in the Ni peaks' FWHM with the change in slope for the CrC lattice strain confirms that matrix yielding is responsible for the internal load transfer to the reinforcement.

The load fraction borne by each phase, $l_p$, can be determined experimentally using Eq. (11):

$$l_p = \frac{f_p \sigma_p}{f_R \sigma_R + f_M \sigma_M} = \frac{f_p \sigma_p}{f_R \sigma_R + (1 - f_R)\sigma_M} \tag{11}$$

Where $f_p$ ($p = R$ *or* $M$) is the phase volume fraction which we measured via SEM micrographs, and $\sigma_p$ is the phase specific stress which can be calculated as a function of the experimentally measured lattice strains and the elastic constants:

$$\sigma_p = \frac{E_{p<hkl>}}{1+\nu} \bullet \varepsilon_{zz} + \frac{\nu E_{p<hkl>}}{(1+\nu)(1-2\nu)} \bullet (\varepsilon_{zz} + \varepsilon_{xx} + \varepsilon_{yy}) \tag{12}$$

Where $\varepsilon_{ii}$ ($i = x, y, z$) is the measured principal lattice strains, $\nu$ is the Poisson's ratio, and $E_{p<hkl>}$ is the directional elastic modulus which is determined using the compliance constants ($S_{ii}$) of respective phases:

$$\frac{1}{E_{p<hkl>}} = S_{11} - (2S_{11} - 2S_{12} - S_{44}) \frac{(h^2k^2 + k^2l^2 + l^2h^2)}{h^2 + k^2 + l^2} \tag{13}$$

The load fractions borne by the matrix are also determined theoretically and numerically using the Eshelby's inclusion models (Eqs. (9) and (10)) and finite element simulations respectively. Fig. 8 compares the experimentally calculated results and the predictions from the Eshelby model and FE simulations. During the elastic stage, both Ni and CrC phases exhibit relatively constant load fractions, consistent with the predictions from the Eshelby's inclusion model and the FE simulation. The relatively high level of engagement from the CrC particles indicates that a reasonably good interfacial bonding between the matrix and the reinforcement was achieved via cold spray. We observe deviations from a constant load fraction once plastic deformation initiates in the Ni phase at an applied stress of around 600 MPa. At this point, the load fraction borne by the matrix decreases. The reduction in the load bearing capacity of the matrix is compensated for by a greater engagement in load bearing from the reinforcement. The trend is also predicted by the FE results as we observe a gradual decrease and increase in the load fraction of the matrix and reinforcement respectively. The experimental measurements show that the load fraction borne by the reinforcement increases up to ~50 % specifically at ~1.1 GPa. This close-to-fracture rise in the ceramic load fraction, which we attribute to matrix and/or interfacial damage evolution, is not captured by the FE simulations as no criterion was included to capture damage processes in the two phases nor at the interface.

## 4. Discussion

Finite element simulation results in Fig. 9a show how the equivalent plastic strain in the matrix evolves during the deformation of the MMC. Localized plasticity, also known as micro-yielding, initiates in the matrix

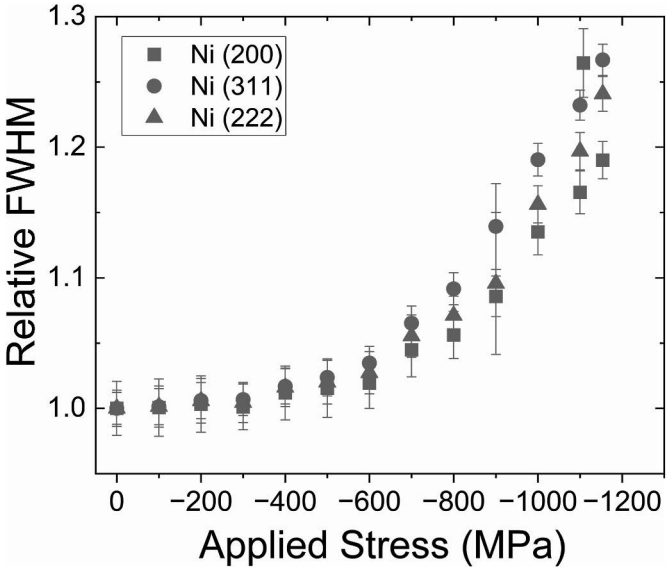


**Fig. 7.** Relative full width half maximum (FWHM) of Ni peaks. There is a clear increase in FWHM once the macroscopic stress exceeds 600 MPa suggesting plastic deformation in the matrix.

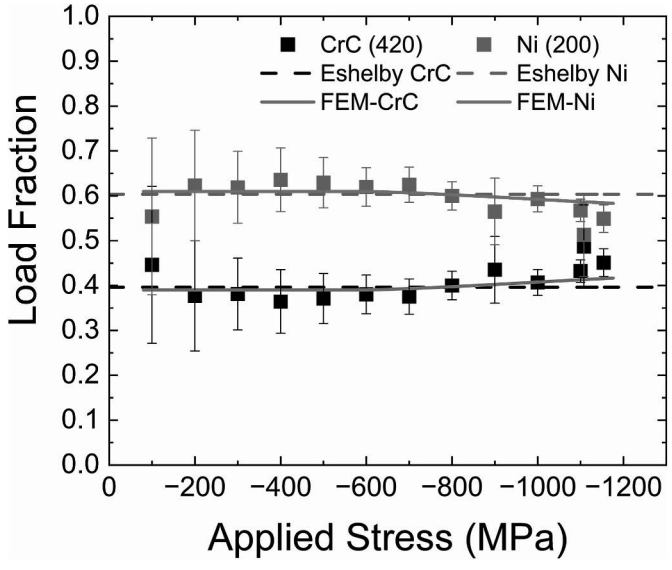


**Fig. 8.** Comparison of load fraction of Ni and CrC calculated from experimental results with those predicted by Eshelby's inclusion model and FE modeling results. Note that the Eshelby inclusion models only predicted the load fractions in the elastic regime.

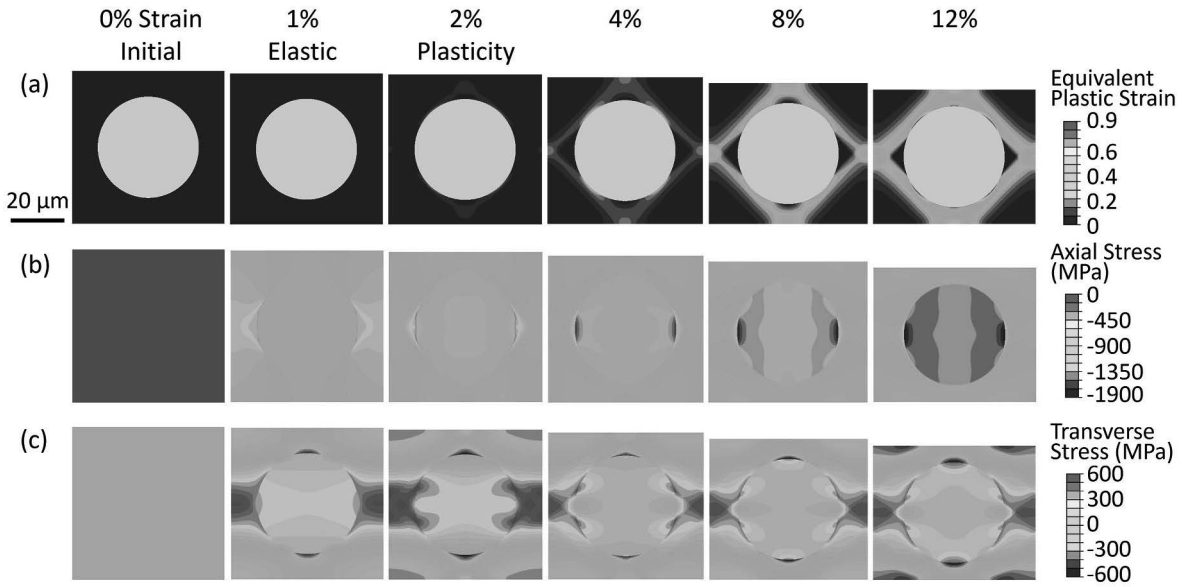


**Fig. 9.** The equivalent plastic strain (a) in a perfectly bonded Ni–CrC composite under compression until 12 % macroscopic strain. Axial (b) and transverse (c) stress distribution are also shown. Positive values indicate tension, while negative values indicate compression. Note that the strengthening effect of reinforcement is clearly shown by the high compressive stress present in the axial direction. However, tensile stress develops in the transverse direction for the matrix between reinforcing particles.

at a global strain of ~0.3 % corresponding to 611 MPa applied stress. For better visualization, here we show the cases when the equivalent plastic strain is at and beyond 2 %. At 2 % strain, we can still observe clear signatures of micro-yielding which is mainly concentrated at matrix/reinforcement interfacial regions to accommodate localized strain gradient. We observe evident global yielding at 4 % strain indicated by the formation of continuous deformation bands around the reinforcing particles shown in Fig. 9a. The thickness of the deformation bands increases upon further straining as does the overall strain within the bands. Global yielding requires a microscopic stress high enough for repeated long-range glide of dislocations throughout the matrix. From a macroscopic perspective, macroscopic flow necessitates interconnected regions of plastic flow such as the band like patterns in Fig. 9a.

Fig. 9b shows the distribution of the axial stress and its evolution with loading. We observe a more uniform state of stress in the reinforcement than the matrix in the elastic regime. The state of stress in the matrix remains nearly constant throughout the deformation once plastic deformation occurs in the matrix. The continued external loading in the plastic regime is accommodated by the reinforcement as evident from the continuous increase in the reinforcement axial stress. These findings align well with the trend of the measured plateau in the Ni axial lattice strain together with the continuous increase in the CrC axial lattice strain shown in Fig. 6. Furthermore, Fig. 9b shows how a reinforcement redistributes stress in its neighborhood. The regions in the matrix between the reinforcements in the transverse direction experience lower levels of axial stress compared to other regions of the matrix. This stress redistribution highlights the role of the load transfer and its impact on the MMC stress states.

The average axial stress in the particle at 12 % strain was predicted to be −1514 MPa in Fig. 9b. To confirm whether this level of axial stress can actually fracture the ceramic particles, we use Eq. (14) proposed by Hiramatsu [49]. This equation correlates the load at which a brittle particle fractures upon compression, to the particle's fractures strength, $S_f$ :

$$F = \frac{\pi d^2 S_f}{2.8} \tag{14}$$

with $d$ being the particle diameter. Taking the fracture strength of CrC particles to be ~1 GPa [50], we expect a fracture load of ~1.54 N for an average particle size of 37 μm. We can determine the experimental fracture loads for the reinforcing particles in the composites using Eq. (15):

$$F_{exp} = \frac{l_R \sigma^A}{f} \frac{\pi d^2}{4} \tag{15}$$

Where $l_R$ and $f$ are the experimentally determined load fraction and volume fraction of the CrC particles, respectively. $\sigma^A$ is the applied stress upon failure of the CrC particles. Consequently, the expected average fracture load for the particles is ~1.6 N which agrees well with that estimated using Hiramatsu's equation and FE results. This confirms that fracture indeed occurs in the CrC particles under stress levels predicted in Fig. 9a and b.

Fig. 9c shows the distribution of the transverse stress and its evolution with loading. We observe a substantial level of tensile stress localized at the matrix/reinforcements interface which can be attributed to the heterogeneous deformation during plastic deformation of Ni. In the elastic regime, the deformation mismatch at the interface is relatively small as Ni and CrC have similar Poisson's ratios (0.31 for the former and 0.3 for the latter). The plastic flow in Ni, however, requires the Poisson's ratio to suddenly increase to 0.5 which in turn causes a significant deformation mismatch at the interface. As a result a high level of transverse stress will be required to accommodate the heterogeneous deformation at the interface. This makes the interface at the beginning of plasticity in the matrix particularly prone to decohesion. The large driving force for interface decohesion suggested by the simulation is in line with the relaxation of transverse lattice strain in Ni (Fig. 6) and large transverse interfacial gaps (Fig. 5) observed experimentally.

In Fig. 10, we schematically summarize the internal load transfer and failure mechanisms in the Ni–CrC MMCs by showing the defect evolution and load fraction variations at different deformation stages. In the elastic regime the fraction of load borne by the matrix and reinforcement remains constant. The existing defects do not have a significant effect on the load partitioning in the elastic regime as our experimental measurements of the load fraction in in the elastic regime are very close to the Eshelby's prediction. The internal load transfers from the matrix to the reinforcement begins with the plastic deformation of the matrix. Our measurements show that the transverse relaxation of the matrix also

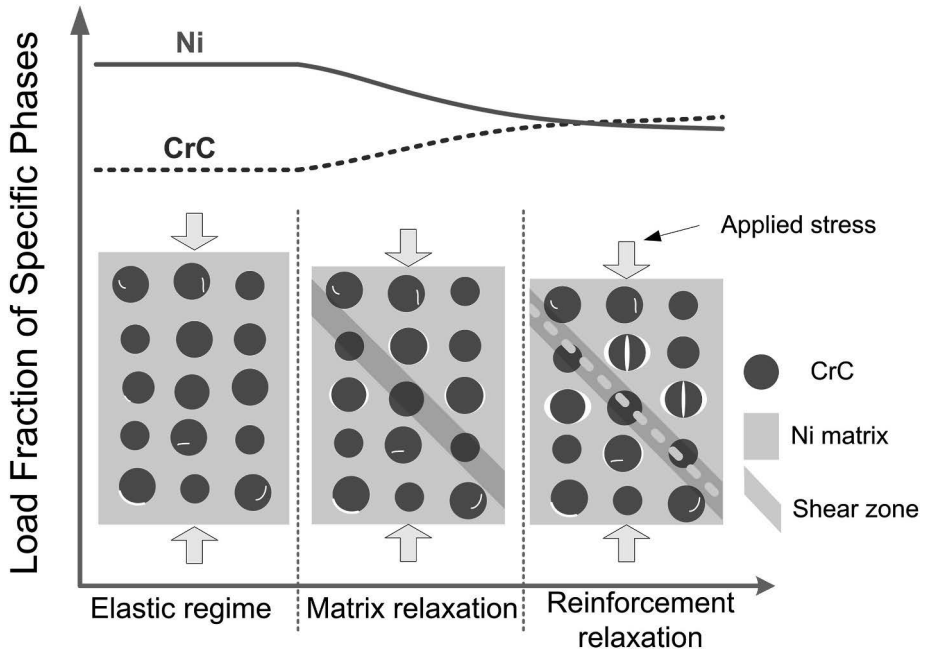


**Fig. 10.** Schematics of defect evolution and internal load transfer process at different deformation stages in Ni–CrC MMC under compressive loading. The small white regions in the elastic and plastic regimes are random cracks. However, the large white regions are cracks formed during the compression loading including particle fracture and interfacial debonding between the Ni matrix and CrC ceramic phases. The shear zone signifies the highly strained zone during compression which eventually leads to failure of the samples. The white dashed line signifies the fracture plane of the composite.

initiates at the same level of applied stress. In principle, matrix relaxation may not necessarily begin with the plastic deformation of the matrix. For example, Bacon et al. [13] reported that matrix relaxation initiated at a stress level exceeding the matrix yield stress by ~300 MPa for stainless steel-$TiB_2$ MMCs. Shi et al. [19] also reported that the onset stress for matrix relaxation was elevated by ~100 MPa compared to the matrix yield stress for Al–TiC particulate MMCs. A higher threshold stress for matrix relaxation compared to the matrix yield stress was also reported for Ti–TiC particulate MMCs [11]. What makes the present MMC distinct is the pre-existing defects due to the cold spray process especially at the matrix/reinforcement interfaces. The imperfectly bonded regions show no apparent resistance to tension once the transverse plastic flow begins in the matrix and therefore matrix/reinforcement decohesion coincides with matrix plastic deformation. Matrix transverse relaxation persists while Ni is plastically deformed to the level that the transverse strain in the Ni phase completely vanishes before the final fracture of the MMC.

The mechanisms through which the cold spray-induced defects intervene with the deformation of MMCs and cause final fracture is different in compression (this work) and tension (our previous work [21]). Pre-existing defects caused a premature elastic fracture in tension before plastic flow begins in the matrix [21]. In compression, on the other hand, as soon as plastic deformation occurs in the matrix, the preexisting defects cause relatively easy lateral decohesion. The lateral decohesion facilitates internal load transfer to the reinforcement to the level that initiates reinforcement fracture followed by the macroscale fracture of MMC immediately afterwards. The use of post-spray thermal and/or mechanical modification techniques can enhance matrix/reinforcement bonding. As a result, matrix/reinforcement decohesion and matrix transverse relaxation can be postponed to stress levels higher than matrix yield strength which we suggest for future studies.

## 5. Conclusion

Deformation of cold sprayed Ni–CrC metal matrix composites under compression was studied using synchrotron X-ray diffraction. A constant load partitioning between the Ni matrix and CrC reinforcement was measured in the elastic regime. The experimental measurements were in line with the Eshelby's inclusion model suggesting a negligible effect of the cold spray-induced defects on the load partitioning in the elastic regime. Internal load transfer from the Ni matrix to the CrC reinforcement initiated with the plastic deformation of the Ni matrix at ~600 MPa applied stress. Lattices strain measurements revealed a transverse relaxation in the matrix taking place at the same time. The matrix/reinforcement interface showed no apparent strength in tension once plastic flow initiated in the Ni matrix. The co-occurrence of matrix plasticity and transverse relaxation can be viewed as the significant effect of the pre-existing defects at the matrix/reinforcement interfaces. The load transfer from the matrix to the reinforcement persisted until the failure of the MMC at ~1.1 GPa. Our results suggest that the failure of the MMC was triggered by the fracture of the reinforcing particles. Resolving the phase-specific response of the Ni–CrC MMC, the internal load transfer and the precursors to final fracture with synchrotron X-ray diffraction should prove useful in the design of structurally reliable MMCs.

## CRediT authorship contribution statement

**Jianxiong Li:** Data curation, Formal analysis, Investigation, Methodology, Visualization, Writing – original draft, Writing – review & editing. **Katherine S. Shanks:** Data curation, Formal analysis, Investigation, Methodology, Writing – review & editing. **Amlan Das:** Data curation, Formal analysis, Investigation, Methodology, Writing – review & editing. **Isaac M. Nault:** Investigation, Methodology, Resources, Writing – review & editing. **Mostafa Hassani:** Conceptualization, Formal analysis, Funding acquisition, Investigation, Methodology, Supervision, Writing – review & editing.

## Declaration of competing interest

The authors declare that they have no known competing financial interests or personal relationships that could have appeared to influence the work reported in this paper.

## Data availability

Data will be made available on request.

## Acknowledgment

J.L. and M.H. gratefully acknowledge funding received from the National Science Foundation (CMMI-2330319). In addition, this work is based upon research conducted at the Center for High Energy X-ray Sciences (CHEXS), which is supported by the National Science Foundation (BIO, ENG and MPS Directorates) under award DMR-1829070. This work also made use of the Cornell Center for Materials Research Shared Facilities which are supported through the NSF MRSEC program (DMR-1719875). The authors would like to thank Qi Tang, Yuan Yao and Lewei He for their help in finite element simulations and the analysis of the XRD results.

## Appendix A. Supplementary data

Supplementary data to this article can be found online at https://doi.org/10.1016/j.msea.2024.146907.

## References

[1] N. Chawla, K.K. Chawla, Metal Matrix Composites, Springer New York, New York, NY, 2013, https://doi.org/10.1007/978-1-4614-9548-2.
[2] J.W. Kaczmar, K. Pietrzak, W. Włosiński, The production and application of metal matrix composite materials, J. Mater. Process. Technol. 106 (2000) 58–67, https://doi.org/10.1016/S0924-0136(00)00639-7.
[3] S. Rawal, Metal-matrix composites for space applications, JOM 53 (2001) 14–17, https://doi.org/10.1007/S11837-001-0139-Z, 2001 53:4.
[4] P. Shiva Shanker, A review on properties of conventional and metal matrix composite materials in manufacturing of disc brake, Mater Today Proc 5 (2018) 5864–5869, https://doi.org/10.1016/J.MATPR.2017.12.184.
[5] A.A. Adebisi, M.A. Maleque, M.M. Rahman, Metal matrix composite brake rotor: historical development and product life cycle analysis, International Journal of Automotive and Mechanical Engineering (IJAME)Online) 4 (n.d.) 471–480.
[6] N. Chawla, Y.L. Shen, Mechanical behavior of particle reinforced metal matrix composites, Adv. Eng. Mater. 3 (2001) 357–370, https://doi.org/10.1002/1527-2648(200106)3:6<357::AID-ADEM357>3.0.CO;2-I.
[7] I.A. Ibrahim, F.A. Mohamed, E.J. Lavernia, Particulate reinforced metal matrix composites - a review, J. Mater. Sci. 26 (1991) 1137–1156, https://doi.org/10.1007/BF00544448.
[8] T.J.A. Doel, P. Bowen, Tensile properties of particulate-reinforced metal matrix composites, Compos Part A Appl Sci Manuf 27 (1996) 655–665, https://doi.org/10.1016/1359-835X(96)00040-1.
[9] J. Nellesen, R. Laquai, B.R. Müller, A. Kupsch, M.P. Hentschel, N.B. Anar, E. Soppa, W. Tillmann, G. Bruno, In situ analysis of damage evolution in an Al/Al2O3 MMC under tensile load by synchrotron X-ray refraction imaging, J. Mater. Sci. 53 (2018) 6021–6032, https://doi.org/10.1007/S10853-017-1957-X, 2018 53:8.
[10] G.G. Sozhamannan, S.B. Prabu, R. Paskaramoorthy, Failures analysis of particle reinforced metal matrix composites by microstructure based models, Mater. Des. 31 (2010) 3785–3790, https://doi.org/10.1016/j.matdes.2010.03.025.
[11] D. Canelo-Yubero, C. Poletti, F. Warchomicka, J. Daniels, G. Requena, Load partition and microstructural evolution during hot deformation of Ti-6Al-6V-2Sn matrix composites, and possible strengthening mechanisms, J. Alloys Compd. 764 (2018) 937–946, https://doi.org/10.1016/j.jallcom.2018.06.097.
[12] M.D.S. Hayat Harshpreet, He Zhen, Cao Peng, Titanium metal matrix composites: an overview, Compos Part A Appl Sci Manuf 121 (2019) 418–438, https://doi.org/10.1016/j.compositesa.2019.04.005.
[13] H. D, E. Bacon Lyndon, James E. Moffatt, Michael E. Fitzpatrick, Synchrotron X-ray diffraction measurements of internal stresses during loading of steel-based metal matrix composites reinforced with TiB2 particles, Acta Mater. 59 (2011) 3373–3383, https://doi.org/10.1016/j.actamat.2011.02.012.
[14] S.G. Roy Jens, Kostov Vladimir, Weidenmann Kay André, Nagel Alwin, Wanner Alexander, Load partitioning study in a 3D interpenetrating AlSi12/Al2O3 metal/ceramic composite, Mater. Sci. Forum 772 (2013) 103–107. https://doi.org/10.4028/www.scientific.net/msf.772.103.
[15] E. Gadalińska, A. Baczmański, S. Wroński, P. Kot, M. Wroński, M. Wróbel, C. Scheffzük, G. Bokuchava, K. Wierzbanowski, Neutron diffraction study of phase stresses in Al/SiCp composite during tensile test, Met. Mater. Int. 25 (2019) 657–668, https://doi.org/10.1007/s12540-018-00218-7.
[16] M. Daymond, M. Fitzpat Rick, Effect of cyclic plasticity on internal stresses in a metal matrix composite, Metall. Mater. Trans. 37 (2006) 1977–1986.
[17] E.B. Gadalińska Andrzej, Wroński Sebastian, Kot Przemysław, Wronski Marcin, Wróbel Mirosław, Scheffzük Christian, Bokuchava Gizo, Wierzbanowski Krzysztof, Neutron diffraction study of phase stresses in Al/SiCp composite during tensile test, Met. Mater. Int. 25 (2018) 657–668, https://doi.org/10.1007/s12540-018-00218-7.
[18] T. Clyne, P. Withers, An introduction to metal matrix composites, Cambridge University Press, Cambridge, 1993.
[19] N.; B, A.M. Shi Mark, J.A. Roberts, John E. Allison, Phase-stress partition during uniaxial tensile loading of a TiC-particulate-reinforced Al composite, Metall. Mater. Trans. 28 (1997) 2741–2753, https://doi.org/10.1007/s11661-997-0031-8.
[20] M.S. Commisso, C. Le Bourlot, F. Bonnet, O. Zanelatto, E. Maire, Thermo-mechanical characterization of steel-based metal matrix composite reinforced with TiB2 particles using synchrotron X-ray diffraction, Materialia (Oxf) 6 (2019), https://doi.org/10.1016/j.mtla.2019.100311.
[21] L. He, D.C. Pagan, A. Nardi, M. Hassani, Synchrotron X-ray diffraction studies of the phase-specific deformation in additively manufactured Ni–CrC composites, Compos. B Eng. 222 (2021) 109086, https://doi.org/10.1016/J.COMPOSITESB.2021.109086.
[22] L. He, Internal load transfer in metal matrix composites revealed by in-situ synchrotron x-ray diffraction, 2022.
[23] S. Roy, J. Gibmeier, K.G. Schell, E.C. Bucharsky, K.A. Weidenmann, A. Wanner, M. J. Hoffmann, Internal load transfer in an interpenetrating metal/ceramic composite material studied using energy dispersive synchrotron X-ray diffraction, Mater. Sci. Eng. 753 (2019) 247–252, https://doi.org/10.1016/j.msea.2019.03.049.
[24] S.G. Roy Jens, Wanner Alexander, In situ study of internal load transfer in a novel metal/ceramic composite exhibiting lamellar microstructure using energy dispersive synchrotron X-ray diffraction, Adv. Eng. Mater. 11 (2009) 471–477, https://doi.org/10.1002/adem.200800352.
[25] S.U. Tang Raghunandan, C. Suryanarayana, Eckert Jürgen, Prashanth Konda Gokuldoss, Zhi Wang, Additive manufacturing of aluminum-based metal matrix composites—a review, Adv. Eng. Mater. 23 (2021) 2100053–NA, https://doi.org/10.1002/adem.202100053.
[26] M.D.S. Hayat Harshpreet, He Zhen, Cao Peng, Titanium metal matrix composites: an overview, Compos Part A Appl Sci Manuf 121 (2019) 418–438, https://doi.org/10.1016/j.compositesa.2019.04.005.
[27] A.L. Mortensen Javier, Metal matrix composites, Annu. Rev. Mater. Res. 40 (2010) 243–270, https://doi.org/10.1146/annurev-matsci-070909-104511.
[28] J.J.M.R. Hillary R, Joseph J. Dixon Jim, Samuel C. Samson Jerold, A study on microstructural effect and mechanical behaviour of Al6061–5%SiC–TiB2 particulates reinforced hybrid metal matrix composites, J. Compos. Mater. 54 (2019) 2327–2337, https://doi.org/10.1177/0021998319894666.
[29] W.S.H.F.J Miller, Strengthening mechanisms in particulate metal matrix composites, Scripta Metall. Mater. 25 (1991) 33–38, https://doi.org/10.1016/0956-716x(91)90349-6.
[30] A.J.; B, A.M. Allen Mark, S. Dawes, M.T. Hutchings, Philip J. Withers, The analysis of internal strains measured by neutron diffraction in Al/SiC metal matrix composites, Acta Metall. Mater. 40 (1992) 2361–2373, https://doi.org/10.1016/0956-7151(92)90155-8.
[31] P. Maurya, N. Kota, J. Gibmeier, A. Wanner, S. Roy, Review on study of internal load transfer in metal matrix composites using diffraction techniques, Mater. Sci. Eng. 840 (2022), https://doi.org/10.1016/j.msea.2022.142973.
[32] D.M. Jafarlou, C. Walde, V.K. Champagne, S. Krishnamurty, I.R. Grosse, Influence of cold sprayed Cr3C2-Ni coating on fracture characteristics of additively manufactured 15Cr-5Ni stainless steel, Mater. Des. 155 (2018) 134–147, https://doi.org/10.1016/j.matdes.2018.05.063.
[33] S.A. Alidokht, P. Vo, S. Yue, R.R. Chromik, Cold spray deposition of Ni and WC-reinforced Ni matrix composite coatings, J. Therm. Spray Technol. 26 (2017) 1908–1921, https://doi.org/10.1007/s11666-017-0636-4.
[34] S.A. Alidokht, P. Manimunda, P. Vo, S. Yue, R.R. Chromik, Cold spray deposition of a Ni-WC composite coating and its dry sliding wear behavior, Surf. Coat. Technol. 308 (2016) 424–434, https://doi.org/10.1016/j.surfcoat.2016.09.089.
[35] M. Verelst, J.P. Bonino, M. Brieu, A. Rousset, Thermomechanical Properties of Ni-A&O, metal matrix composites produced by electroforming, 1995.
[36] T.B. Torgerson, M.D. Harris, S.A. Alidokht, T.W. Scharf, S.M. Aouadi, R. R. Chromik, J.S. Zabinski, A.A. Voevodin, Room and elevated temperature sliding wear behavior of cold sprayed Ni-WC composite coatings, Surf. Coat. Technol. 350 (2018) 136–145, https://doi.org/10.1016/j.surfcoat.2018.05.090.
[37] R. Karmakar, P. Maji, S.K. Ghosh, A review on the nickel based metal matrix composite coating, Met. Mater. Int. 27 (2021) 2134–2145, https://doi.org/10.1007/s12540-020-00872-w.
[38] A. Roatta, R.E. Bolmaro, An Eshelby inclusion-based model for the study of stresses and plastic strain localization in metal matrix composites I: general formulation and its application to round particles, Mater. Sci. Eng. 229 (1997) 182–191.
[39] J.D. Eshelby, The determination of the elastic field of an ellipsoidal inclusion, and related problems, Proceedings of the Royal Society of London. Series A 241 (1957) 376–396. https://royalsocietypublishing.org/.
[40] P.J. Withers, W.M. Stobbs, B. Pedersen, The application of the eshelby method of internal stress determination to short fibre metal matrix composites, 1989.
[41] D. Huda, M.A. El Baradie, M.S.J. Hashmi, Analytical Study for the stress analysis of Metal Matrix Composites, 1994.
[42] D.H. Bacon, L. Edwards, J.E. Moffatt, M.E. Fitzpatrick, Synchrotron X-ray diffraction measurements of internal stresses during loading of steel-based metal matrix composites reinforced with TiB2 particles, Acta Mater. 59 (2011) 3373–3383, https://doi.org/10.1016/j.actamat.2011.02.012.
[43] T.E. Wilkes, B.J. Harder, J.D. Almer, K.T. Faber, Load partitioning in honeycomb-like silicon carbide aluminum alloy composites, Acta Mater. 57 (2009) 6234–6242, https://doi.org/10.1016/j.actamat.2009.08.050.
[44] E. Gadalińska, A. Baczmański, S. Wroński, P. Kot, M. Wroński, M. Wróbel, C. Scheffzük, G. Bokuchava, K. Wierzbanowski, Neutron diffraction study of phase stresses in Al/SiCp composite during tensile test, Met. Mater. Int. 25 (2019) 657–668, https://doi.org/10.1007/s12540-018-00218-7.

[45] A. Khennane, Introduction to Finite Element Analysis Using MATLAB ® and Abaqus, CRC Press, 2013.
[46] S. Sayahlatifi, C. Shao, A. McDonald, J. Hogan, 3D microstructure-based finite element simulation of cold-sprayed Al-Al2O3 composite coatings under quasi-static compression and indentation loading, J. Therm. Spray Technol. 2021 (2021) 1–17, https://doi.org/10.1007/S11666-021-01260-5.
[47] M. Vashista, S. Paul, Correlation between full width at half maximum (FWHM) of XRD peak with residual stress on ground surfaces, Phil. Mag. 92 (2012) 4194–4204, https://doi.org/10.1080/14786435.2012.704429.
[48] M. Lindgren, T. Lepisto, Effect of prestraining on Barkhausen noise vs. stress relation, NDT&E International 34 (2001) 337–344. www.elsevier.com/locate/ndteint.
[49] Y. Hiramatsu, Y. Oka, H. Kiyama, Rapid determination of the tensile strength of rocks with irregular test pieces, J. Mining. Metallurgic. Inst. Jpn. 81 (1965) 1024–1030.
[50] CAS Number: 12012-35-0. Physical Form: Gray Orthorhombic Crystals, (n.d.). https://www.matweb.com/search/DataSheet.aspx?MatGUID=c5b65890d6e74820a40b517269185cbf (accessed August 1, 2023).